

## TITAN DR1: An Improved, Validated, and Systematically-Controlled Recalibration of ATLAS Photometry toward Type Ia Supernova Cosmology

ELIJAH G. MARLIN,<sup>1</sup> YUKEI S. MURAKAMI,<sup>2</sup> DILLON BROUT,<sup>1</sup> JACK W. TWEDDLE,<sup>3</sup> BRODIE POPOVIC,<sup>4</sup> KEN SMITH,<sup>4</sup> STEPHEN SMARTT,<sup>3</sup> DANIEL M. SCOLNICK,<sup>5</sup> DAVID JONES,<sup>6</sup> ERIK R. PETERSON,<sup>7,8</sup> ADAM G. RIESS,<sup>2,9</sup> MARIA VINCENZI,<sup>3</sup> JASPER MILSTEIN,<sup>1</sup> AND MITCHELL DIXON<sup>6</sup>

<sup>1</sup>*Departments of Astronomy and Physics, Boston University, Boston MA 02215*

<sup>2</sup>*Department of Physics and Astronomy, Johns Hopkins University, Baltimore, MD 21218, USA*

<sup>3</sup>*Astrophysics sub-Department, Department of Physics, University of Oxford, Keble Road, Oxford, OX1 3RH*

<sup>4</sup>

<sup>5</sup>*Department of Physics, Duke University, Durham, NC 27708, USA*

<sup>6</sup>*Institute for Astronomy, University of Hawaii, 640 N. Aohoku Pl., Hilo, HI 96720, USA*

<sup>7</sup>*Department of Physics, University of Michigan, Ann Arbor, MI 48109, USA*

<sup>8</sup>*Society of Fellows, University of Michigan, Ann Arbor, MI 48109, USA*

<sup>9</sup>*Space Telescope Science Institute, 3700 San Martin Drive, Baltimore, MD 21218, USA*

### ABSTRACT

ATLAS (Asteroid Terrestrial Last Alert System) is a transient survey of four telescopes covering the entire sky. It has observed over 10,000 spectroscopically confirmed Type Ia supernovae (SNe Ia), with thousands of cosmology-grade light curves (to be released as TITAN DR1). To prepare this massive, low-redshift dataset for cosmology, we evaluate and cross-calibrate ATLAS forced photometry using tertiary stars from the DES (Dark Energy Survey) Y6 release. The 5000 deg<sup>2</sup> DES footprint overlaps regions both in and out of the PS1 (Pan-STARRS DR1) footprint, allowing tests of the primary calibrator for the ATLAS Refcat2 catalog. Initial offsets are at the ∼40 mmag scale. To improve this we determine Δzeropoint offsets for two cases: (1) pixel-to-pixel offsets within individual CCDs (reduced from ∼8 to ∼4 mmag RMS) and (2) chip-to-chip offsets across the 9 CCDs and filters (reduced from ∼17 to ∼3 mmag RMS). We also identify the largest systematic uncertainty as a transmission-function color dependence, requiring shifts in the assumed ATLAS filters at the ∼30 mmag level if uncorrected. We validate our calibration using (a) CALSPEC standards, (b) an independent tertiary catalog, and (c) distance moduli of cross-matched SNe Ia, all showing improved consistency. Overall, we estimate combined calibration-related systematics at the ∼5–10 mmag level, supporting competitive cosmological constraints with the TITAN SN Ia dataset.

**Keywords:** Cosmology, cosmology: observations, (stars:) supernovae: general

### 1. INTRODUCTION

Type Ia supernovae (SNe Ia), thermonuclear explosions of white dwarf stars, are one of the most successful standardizable candles thanks to their known luminosity-color-duration relationship (Phillips 1993; Hamuy et al. 1996; Tripp 1998). The small scatter in the post-standardization luminosity makes SNe Ia an excellent distance indicator for cosmology (e.g., Filippenko 2005). The state-of-the-art measurements of cosmological parameters, including the equation of state for dark energy (e.g., DESI Collaboration et al. 2025), use

a compilation of SNe Ia samples that cover a wide range of redshifts, such as DESY5, Pantheon+, and UNION3.

A commonality among these datasets is that they combine low-redshift ( $z \lesssim 0.1$ ) and high-redshift ( $z \lesssim 1$ ) surveys. All SNe Ia datasets used in DESI Collaboration et al. (2025), DES (1500 high-z SNe Ia; Abbott et al. 2024a), UNION3 (containing more than 2000 high-z SNe Ia; Rubin et al. 2025) and Pantheon+ (1550 high-z SNe Ia; Brout et al. 2022; Scolnick et al. 2022a) take advantage of overlapping low-z datasets which add up to ∼200 SNe Ia, (e.g., CfA1; Riess et al. 1999, CfA2; Jha et al. 2006, CfA3-Keplercam; Hicken et al. 2009a, CfA3-4Shooter; Hicken et al. 2009b, CfA4p1, CfA4p2; Hicken et al. 2012, CSP DR3; Krisciunas et al. 2017, LOSS1; Ganeshalingam et al. 2010, LOSS2; Stahl et al. 2019,

Corresponding author: Elijah G. Marlin, Yuwei S. Murakami  
Email: emarlin@bu.edu, ymuraka2@jhu.edu

SOUSA; Brown 2014, Foundation; Foley et al. 2018b, CNia0.02; Chen et al. 2022). Current constraints of cosmology (Boruah et al. 2020; Riess et al. 2022; Scolnic et al. 2022b; Vincenzi et al. 2024, e.g.) rely on these historical low- $z$  SN Ia datasets to point to interesting new physics (Brout et al. 2022; Abbott et al. 2024b; DESI Collaboration et al. 2025; Tang et al. 2025, e.g.). This reliance on existing low- $z$  datasets is problematic, 1). because the relative number of low- $z$  SNe Ia to the expanding high- $z$  datasets remains constant, and 2). this means that all SNe Ia are unknowingly cross correlated and have no solution to remove this correlation. These will continue to be challenges for harnessing the full potential of upcoming high- $z$  surveys, such as LSST (Foley et al. 2018a) and Roman (Sanderson et al. 2024), and necessitates the collection and analysis of new datasets, collected over many years.

TITAN (Type Ia supernova Trove from ATLAS in the Nearby universe), the low- $z$  SN Ia dataset that we present in a series of papers will provide a solution. TITAN is a compilation of spectroscopically confirmed SNe Ia observed by the Asteroid Terrestrial-impact Last Alert System (ATLAS) (Tonry et al. 2018). ATLAS, a NASA funded all sky survey, visits the whole sky every night with limited magnitudes at  $g \sim 20$  mag, making it optimal for capturing low- $z$  SNe Ia up to  $z \lesssim 0.1$ . The first data release of the TITAN dataset, containing  $\sim 10,000$  light curves ( $\sim 3000$  cosmology grade with host- $z$ ) consists of three papers. The overview, SN Ia light curves, and the Hubble diagram are presented in Murakami et al. (2025) and the simulation and the forward-modeling of observational bias is presented in Tweddle et al. (2025). In this paper, we validate the ATLAS calibration and implement literature standard corrections in preparation for cosmological analysis. In our Gold SNe Ia sample, we find a scatter of  $\lesssim 0.17$  mag.

The calibration of datasets, such as Pantheon+, consist of two steps: characterization of surveys' photometric systems (e.g., uniformity of the focal plane, temporal changes in transmission properties, linearity along wavelength and flux levels) and correction for each filter/ detector configuration to a single reference photometric system. Scolnic et al. (2015) (supercal) calculate relative zeropoint offsets using secondary (CALSPEC) stars between PS1 (Pan-STARRS DR1) and other telescope systems. This method was updated and improved upon in Brout et al. (2022) (fragalistic) for Pantheon+, through the use of tertiary standards in addition to primary and secondary stars. Additionally, they quantify the small variations of transmission functions and its impact on cosmology. Popovic et al. (2025) (dovekie) is the most recent iteration of this method, providing an

open source framework and expanded sets of primary calibration stars with faint DA white dwarf stars.

For calibration of TITAN, we employ the same techniques to cross-check consistency of the existing ATLAS calibration. ATLAS is a telescope network comprised of four telescopes, two in the Northern Hemisphere in Hawaii (Dec  $\geq -50^\circ$ ), and two in the Southern Hemisphere in South Africa and Chile (Dec  $\lesssim +40^\circ$ ) (Tonry et al. 2018). Of these, the northern telescopes underwent several changes and upgrades of detector setups, resulting in nine total telescope/ CCD combinations, over a decade, since commissioning. ATLAS primarily uses two broadband filters: ATLAS-cyan ( $4200 \lesssim \lambda_{\text{obs}} \lesssim 6500\text{\AA}$ ) and ATLAS-orange ( $5600 \lesssim \lambda_{\text{obs}} \lesssim 8200\text{\AA}$ ) (Tonry et al. 2018). In total, we have 18 possible filter-detector configurations (e.g., chip 0 - cyan = chip 0c), with exceptions of chips 0 and 2 not containing cyan (see Tab. 1 for chip details). In this work we treat each combination as separate filters (similarly to CfA filters in supercal).

The baseline ATLAS calibration, applied to every frame by default, uses Refcat2, an all-sky tertiary star catalog in the PS1 system (Tonry et al. 2018). Refcat2 is comprised of photometry from eight distinct stellar surveys, primarily PS1, GAIA DR2, and APASS. The magnitude of each star is calculated as the average magnitude from each survey that observes it. In this work, we use an independent, well-calibrated tertiary star catalog, that covers declination ranges inside and outside PS1 to validate the baseline calibration with Refcat2. We select DESY6 tertiary star catalog (Rykoff et al. 2023). The DES survey is known to have a photometric uniformity of  $<1.8$  mmag and, whose absolute flux is known at the 1% level, making it an excellent candidate for a relative calibration. The footprint of 5000 square degrees also provides a wide range of stellar photometry (with over 17 million observed stars) for us to cross compare with, which is needed given the all sky nature of ATLAS.

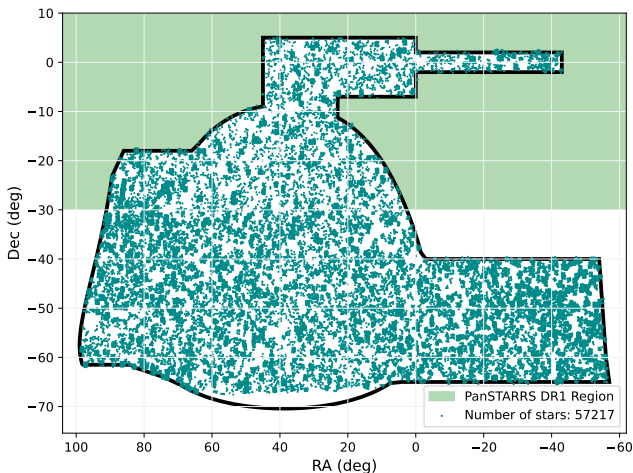
We present the data used in this work, including ATLAS, DES, and synthetic photometry in Sec. 2. In Sec. 3, we quantify and discuss two levels of calibration (intra-chip, inter-chip) needed to prepare TITAN for cosmology. We compare the resulting SN Ia luminosities with other modern low- $z$  datasets in Sec. 4. We discuss the implications of our findings and their impact on cosmology in Sec. 5, followed by our concluding results in Sec. 6.

## 2. DATA PREPARATION

### 2.1. Tertiary Star Samples

For this paper, we build three distinct tertiary star catalogs. First, a baseline sample of randomly dis-

ID	Sitecam	Nickname	MJD <sub>min</sub>	MJD <sub>max</sub>
0	01a	acam2	57800	58715
1	01a	gold	58719	59465
2	01a	green+fuzzy+4x	59466	59830
3	01a	magenta+wormy+5x	59830	-
4	02a	acam1	57800	58717
5	02a	red	58718	59519
6	02a	red+alien+1	59522	-
7	03a	blue+cruddy+2	59561	-
8	04a	gold+freckles+3x	59605	-

**Table 1.** Detector configurations

**Figure 1.** Each individual star field by RA and Dec. Forced photometry from ATLAS is initially in a 0 to 360 degrees RA range and are converted to a 180 to -180 RA range for consistent plotting. The DES footprint is over plotted here as well as the Pan-STARRS region. Note that the southern telescopes take over slightly below the PS1 region at Dec of -50. Stars were chosen in 1 square degree chunks randomly distributed throughout the DES footprint. There are 500 chunks each containing roughly 200 stars in our color-blind sample, and about 50 stars over 500 chunks in our blue sample. In total there are roughly 125,000 stars collected, although this number gets reduced substantially after cuts.

tributed stars that are common to both Refcat2 and the DES Y6 catalog (Bechtol et al. 2025). This sample has no preference in color or location: the resulting distribution of these stars are not even across color, and exist in small populations at  $g - i$  color  $\leq 0.2$ , resulting in few stars in the blue. Referred to hereafter as 'color-blind' sample. Second, a subset of the catalog above (common Refcat2 and DES Y6 stars) but only for stars that are blue biased ( $DES\ g - i$  color  $\leq 0.2$ ). We use

this second sample because our SNe Ia primarily exist in this color range, and it enables us create a uniform in color, total star catalog, for calibration. Referred to hereafter as 'blue' sample. Third, a baseline sample of randomly distributed stars from DES Y6 that are NOT found in the Refcat2 catalog. These stars functionally similar to SNe Ia, an object whose color and brightness is not used in any part of ATLAS calibration (including initial Refcat2 zeropoint calibration). Referred to hereafter as 'non-refcat' catalog.

For all samples we apply cuts as recommended by the ATLAS team in Tonry et al. (2018). We also apply cuts on stars with excessively large errors (flux  $\geq 2000\mu j$ ),  $\chi^2$  above 5, and  $17 \leq DES\ r$  band  $\leq 19$  mag.

Fig. 1 shows the locations of the blue + color-blind samples. This figure only includes stars that pass cuts and are used in calibration. Note the even distribution of stars across the DES footprint, with the exception of the absolute lowest section.

Now that we have assembled these three catalogs, we proceed to re-sample our tertiary stars catalogs. We re-sample blue + color-blind catalogs, resulting in a roughly even number of stars above and below DES  $g - i$  color of 0. This re-sampled stellar dataset is used in Sec. 3.2. This re-sampling is important because we measure the slope of our observed - synthetic data residual as a function of color for these stars. Having an even distribution of stars across the entire color range is important to avoid bias or not account for slope at a certain color.

Another aspect that is included in the re-sampling is to remove all stars that only contain measurements made by GAIA in Refcat2. We observe a substantial anomaly, particularly at blue colors, in stars observed by GAIA and that have data from no other survey, relative to PS1 stars (which we take as truth). Because of this, and because stars from all other surveys that comprise Refcat2 follow the PS1 trend, we remove these stars from calibration. Additionally, all of these GAIA stars have large error bars. This resolves a potential chromatism at blue colored stars that could bias calibration later on.

## 2.2. ATLAS Forced Photometry

We take our three catalogs and obtain their ATLAS observations by performing the standard forced photometry routine (`tphot`). `tphot` is a custom point-spread-function (PSF) fitting routine: it runs on the difference images of ATLAS forced photometry to produce flux measurements of any source detected  $5\sigma$  or more above noise level. ATLAS forced photometry is run directly

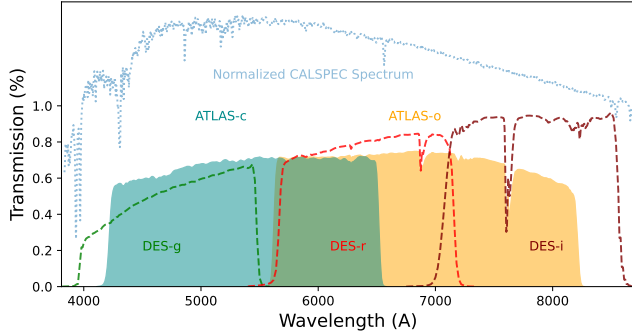


**Figure 2.** Transmission (as a percentage of light allowed) vs wavelength for ATLAS orange and cyan bands vs the DES  $g$ ,  $r$ ,  $i$  bands. Data comes from SVO2. Over plotted is one of the CALSPEC synthetic stars used in our calibration. The star’s flux density is scaled up arbitrarily, to be visible on the same scale as the filter functions. The y-axis (percentages) values associated with it are relative and not absolute.

on the ATLAS server side. There is no proper-motion involved in these requests.

### 2.3. DES Photometry

The DES Y6 survey (Rykoff et al. 2023) is an incredibly robust ( $<2$ mmag relative uniformity over the survey region) and well measured survey, covering a large 5000 square degree portion of the sky. Most of the 17 million stars contained within DESY6 have  $i$ -band magnitude:  $16 < i < 21$ . The survey uses a modification of Foward Global Calibration Method (FGCM) from Burke et al. (2017) to remove positional discrepancies across the DE-Cam CCD.

The absolute calibration is done with the Hubble Space Telescope (HST) CALSPEC standard star *C26202* as specified by Rykoff. Including systematic errors, DES calibrates to *C26202* to the 1% level.

### 2.4. Synthetic Data

We generate synthetic ATLAS and DES photometry with NGSL templates (Koleva & Vazdekis 2012) and CALSPEC standard stars. We take transmission functions for ATLAS from Tonry et al. (2018). We do this by fitting a spectrum of a CALSPEC or NGSL star, to our filter functions wavelength grid. We then integrate this spectrum flux in the photon count space (as opposed to the energy space), and convert this to AB magnitude at the photon pivot wavelength, where AB mag has to be defined in the frequency space. In order to do this at a large scale, we modified the code from Popovic et al. (2025) to include the ATLAS filter functions. This enables us to produce synthetic stars for all of our filters at different wavelength shifts quickly.

### 2.5. ATLAS CCD - Filter System

ATLAS’s 9 CCDs across two filters, produce 18 total CCD-filter configurations. Chip 0 and 2 never took data in the cyan band, leaving us 16 total CCD-filter configurations. The four telescopes that comprise ATLAS began operating about a decade ago with the first northern telescope starting operation in June 2015 (HKO), the second in February 2017 (LMO), the two southern telescopes began operation in 2021. A critical addition was made to the northern telescopes in 2017, as such we were instructed to only use data after MJD 57800. Fig. 2 shows the flux density of each ATLAS and DES filter as a function of wavelength, with a reference CALSPEC stellar spectrum. We observe that ATLAS’s coverage approximately lines up with DES  $g, r, i$  bands.

Another key note is that the quantum efficiency (QE) is not uniform across the two northern telescopes. It is essentially uniform until  $\lambda = 6500\text{\AA}$ , where there is deviation over the rest of the wavelength we use. We do not attribute substantial effects in our calibration with QE. See Fig. 3 in Tonry et al. (2018) for additional details about QE in ATLAS.

## 3. ANALYSIS

We break our calibration down into two primary components. First, we have the intra-chip calibration, where we have examined CCDs of each telescope systematically, to determine pixel to pixel trends that we can correct. Second, is inter-chip calibration. We looked at trends across all filter-chip combos to produce a median  $\Delta$  zeropoint offset for each. This portion also includes filter shifts in wavelength, where we shift the filter by some small amount of  $\text{\AA}$ , to correct for chromatic effects. We conduct this filter shift in a phenomenological manor, focusing primarily on its effects for calibrating for cosmology.

### 3.1. Intra-Chip Variation

The untargeted, all-sky survey pattern by ATLAS creates a dither pattern around each star’s coordinate. This pattern provides an insight into the sensitivity function’s possible variations within each CCD, as the same object is measured at different CCD coordinates.

ATLAS CCDs have 10000X10000 pixels, and each image is read out in 1x1-binning by default. With the median seeing of  $0.5''$  (Lyman et al. 2020), this spans approximately one pixel. The `tphot` forced photometry routine reports the CCD coordinates ( $x, y$ ) that correspond to the requested sky coordinates for the forced photometry. We use this information to construct the coordinate-dependent zeropoint offset map within each chip.

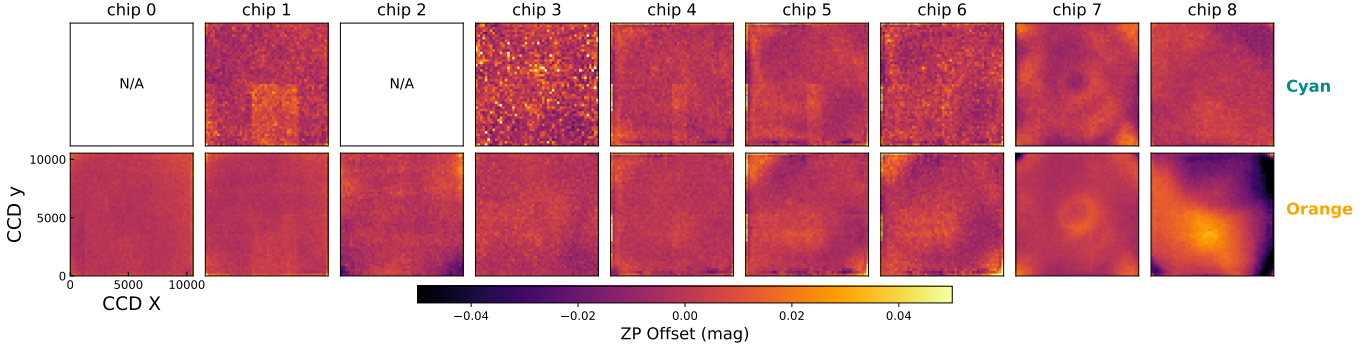


**Figure 3.** The magnitude residual for all chips by pixel. Median binning applied (50 pixel bins). The heat in these plots have the median residual of each chip subtracted out of them to align the chips residual at 0. The purpose of this part of the calibration is to notice pixel to pixel variations, thus having a constant mag offset does not show much, this allows us to more clearly see discrepancies. Note the right side of chip 8. Chip 8 sees a substantial increase in brightness as x pixel moves right. All other chips look relatively uniform, there are some clear CCD patterns (chip 7, 1) across filters that we can still see post zeropoint calibration.

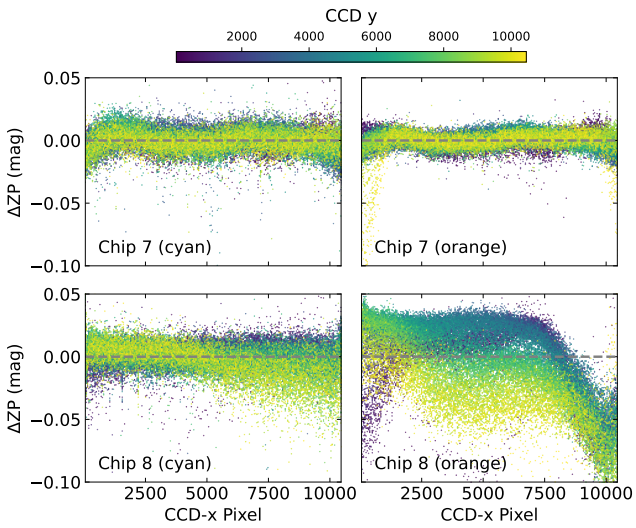


**Figure 4.** Sliced view of two chips from Fig. 3 in orange and cyan bands. The delta in zeropoint in magnitude is shown on the y axis and the x axis is the x pixel. This shows the significant non uniformity of chip 8o as a function of x pixel. Note how in cyan, although not quite as tight as chip 7 there is no pixel dependent non-uniformity. Chip 7 is a much more typical chip, a tight consistent offset centered at 0 (this oscillation pattern seen here in chip 7, can be seen in the chip 7 heatmap as the circular ring). The sharp dips, especially in chip 7o, on the edges of the chip (50 pixel edge) get cut out when we create the correction function.

The procedure is the following: for any given star, we have multiple observations across different x,y coordinates in multiple CCDs. Then for any star with data in a given CCD, we take the median of all magnitude values, and subtract that from each individual pixel to pixel magnitude value. This creates a coordinate dependent offset of one star mapped across all chips. We then repeat for every star and layer the results. Fig. 3 shows

the results of this process. Because we are looking for a coordinate dependence, we subtract out the median offset from each chip, to make net offset 0 if there is no coordinate dependence. We are ignoring edge effects on all the chips as those are notoriously unreliable across CCDs, thus they are cut out, at the 50 pixel scale, before correcting.

Fig. 3 shows chips 0-7 have no particularly concerning patterns, i.e. pixel to pixel variation. We can see some distinct patterns on the 1 mmag scale, even post Refcat2 zeropoint calibration, in chips 1, 4, 7, in both filters. Since these are different filters and thus, completely independent datasets, this is a strong validation that these patterns (and thus those more significant like chip 8o) are physical, and not a product of our data processing.

Chip 8o has a significant vignetting pattern toward the right side. In chip 8o we can see brighter magnitude residuals toward the right side and slightly at the top of the chip. Fig. 4 shows a scatter plot of the x and y axis of chip 1 on the top plots, and the same plot except for chip 8 on the bottom. Clearly visible here is the trend in the x axis of the chip toward brighter observations on the right. A significant observation from Fig. 4 is that this vignetting pattern, producing brighter observations in chip 8o, only exists in the orange band.

We account for this vignetting pattern in our correction model, allowing us to use chip 8o despite its large aberration. We create the correction model by binning the pixels of each chip into 50 pix bins. We use our calculated 'optimal smoothing radius' of 540 pixels (App. C), to convolve our 2D arrays using python's `Gaussian2DKernel`. This convolution then gets remapped to the entire 10,000 by 10,000 pixel space to produce a complete correction map for one chip. Our

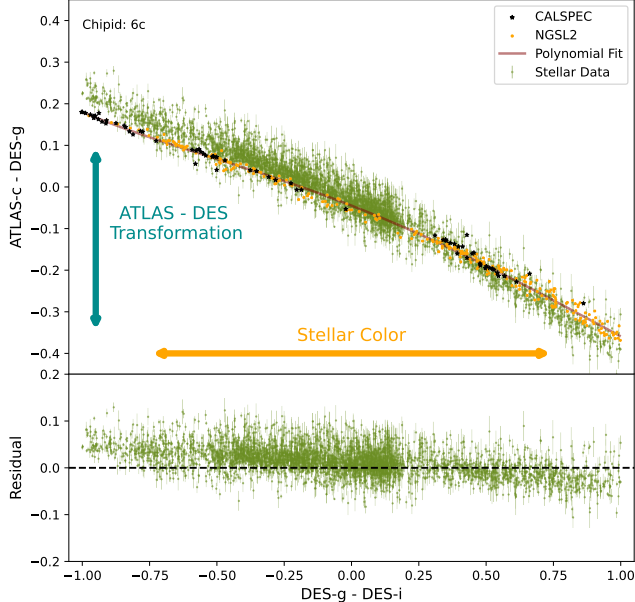


**Figure 5.** ATLAS - DES transformation (ATLAS-c - DES-g) on the y axis with DES color on x axis. Real stellar data (green), over plotted with NGSL and CALSPEC synthetic stellar photometry. Bottom plot is the synthetic - real residual plotted on the y axis. The lower residual plot, shows the chromatic slope that must be accounted for, while the net vertical shift of the green points from the trend line shows the inter-chip offset. A 5th order polynomial is fit to the synthetic data (brown) to show its shape. This specific plot is for chip 6c. The vertical shift used to calculate the offset of each chip-filter combo, is the real data - the synthetic trendline at that x coordinate shown in this plot. The actual calculation is substantially more complex than what is shown here, please see App. A for details. Note: this is the most obvious example of our need for correction, see Fig. 7 for the result of the residuals across all chips.

model applies unique corrections to each chip and each filter separately (16 total correction maps). These maps are then merged together and applied to our calibration. This comprises the intra-chip correction.

### 3.2. Inter-Chip Variation

The inter-chip offset is described as the vertical shift between the observed ATLAS - DES transformation and the synthetic transformation in Fig. 5. The residual plot on the bottom of this figure shows the value of this vertical shift as a function of DES color. The residual is calculated as the y axis difference between the real data at that color and the synthetic polynomial. The synthetic polynomial is a 5th order approximation of the synthetic data using python’s `Polynomial.fit`.

We expect that this residual is a flat line centered away from 0. The amount this line is offset from 0 would be the zeropoint offset of this chip-filter combination (there

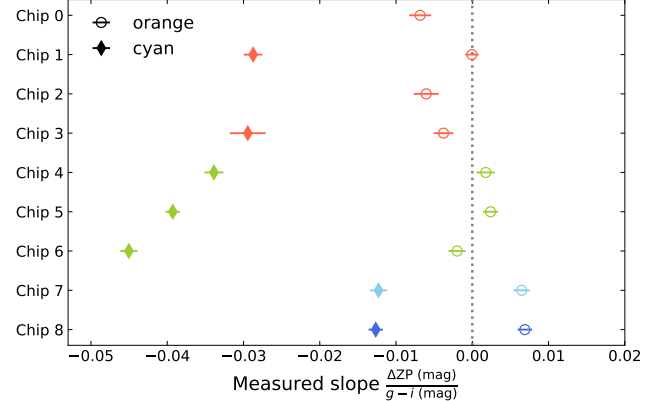


**Figure 6.** Whisker plot, with chip on the y axis and the measured slope of the residual (shown at the bottom of Fig. 5) on x axis. On x axis,  $\Delta ZP$  represents the mean offset between real ATLAS - DES data and synthetic which can be seen visually in Fig. 5. Colored by which telescope each chip corresponds to. Orange band is tightly packed around no slope, with an average close to 0. Cyan band is consistently negative sloped, indicating a chromatic offset. Chips 4,5,6 (all same telescope over time) get progressively worse, this could indicate a physical problem with the filter that worsens each time the CCD is switched. Chip 7,8 represent the newer 2021 telescopes, and have a much smaller slope, potentially the result of a correction to the cause. The larger the slope value the larger the wave shift we apply, thus, this plot, indicates the significance of the shift.

is a collapsed likelihood function used here to generate this, but it is still the result of this residual). This is the zeropoint offset because the synthetic data uses CALSPEC stars, which have the absolute flux of our filter function.

Notably, there is a  $g - i$ -color dependent trend in the residuals. Considering that this is a residuals of observed photometry from the synthetic photometry, the presence of slope implies that our the filter transmission function used for the synthetic photometry differ from each telescope-detector-filter combinations’ actual throughput. This is not an unusual observation: previous cosmology-grade calibrations of SNe Ia catalogs, such as Brout et al. (2022) and Popovic et al. (2025) have identified the slopes using a similar method. Unless a careful, laboratory-level re-measurement of the system throughput can be immediately performed, these slopes are typically corrected by applying modifications to each filter’s transmission function. Fig. 7 demonstrates the color-dependent (chromatic) effect of such modifications: two distinct methods (wavelength-shift and filter-tilt; see Popovic et al. 2025 for review) produce a nearly identical color-dependent change in the predicted magnitudes. For consistency with the literature and simplicity, we choose to employ the wavelength-

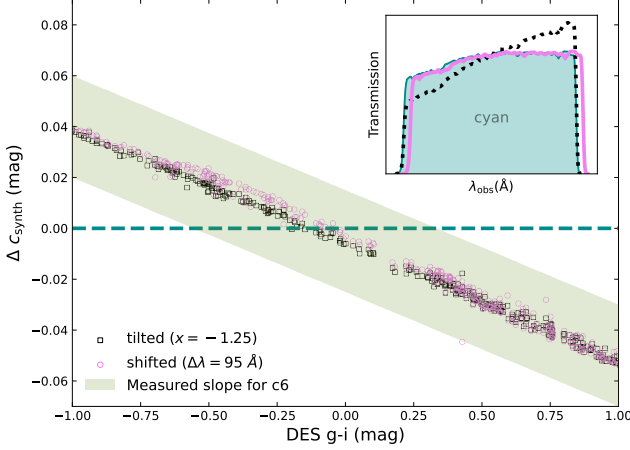


**Figure 7.** This shows results for chip 6c, the same chip in Fig. 5. The Y axis is the synthetic magnitude of cyan band with no shift minus the magnitude with a shift, showing how we shift our synthetic values at each color. X axis is DES g-i color. A green line is over plotted to show the observed slope in the residuals. The subplot in the top right corner shows the original, shifted, and tilted transmission functions. The tilt is -1.25 and the shift here is 95 Å. Note, this is a particularly intense slope, see Fig. 7 for the all slope values.

shift method. A correct choice of wavelength shift can match the measured slope in the tertiary stars, essentially mitigating the chromatic effect during the light-curve fitting of the cosmological SNe Ia samples.

The results of applying this shift means, that, in cyan we shift each chip by approximately 50 - 100 Å in the same direction. Although this initially sounds substantial, given how broad the ATLAS filter bands are this would essentially be the equivalent of shifting a DES band 25 - 50 Å. Still, shifting a filter function this much is not physical, it can result in shifting through telluric lines for example. While we understand this is not the physical solution to the chromatic slope, we take a phenomenological approach because this approximation fits extremely well, and is backed up in the literature as a viable solution for cosmology.

### 3.3. Reference Catalog Validation

For each forced photometry image we collect from ATLAS there is a zeropoint calculated using stars from the Refcat2 catalog. This catalog is a combination of many different surveys to get an all sky coverage that corresponds to ATLAS. The primary surveys involved here are PS1 and GAIA (Tonry et al. 2018).

We validated that no single survey was providing chromatic or skewed data results, thus biasing our photometry. The Refcat2 catalog combines every survey that measures a star and averages their magnitudes together, as such, there is no clean way to determine the compo-

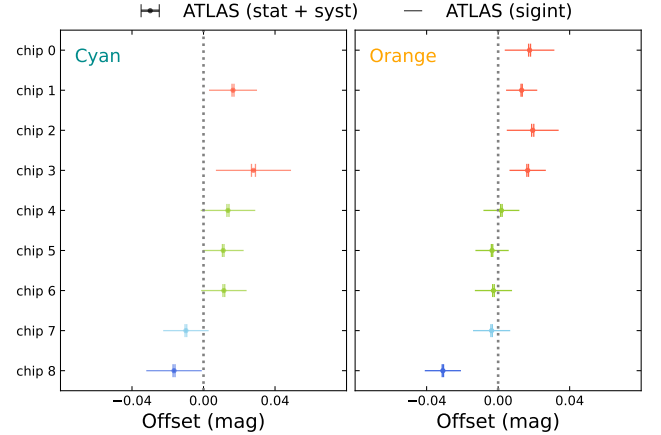


**Figure 8.** Chip on y axis and offset in magnitude on x axis, in the orange and cyan bands in ATLAS. This offset is the vertical shift of the real data from the synthetic data in ATLAS-DES transformation vs color, as demonstrated in Fig. 5. This is condensed down to a single value across multiple colors and DES filters. See Sec. A for details. Two error bars are displayed here, one (small) representing the statistical error in the physical ATLAS data, and the other (large) representing corresponding to the dispersion of the data (intrinsic scatter).

nent only one survey contributes to that result. Thus, we look mostly at stars that only have contribution from one survey, or are specifically missing contribution from one survey. Our primary finding is that, in the blue region, stars that are only measured by GAIA are skewed substantially off the main PS1 branch. This could result in a bias from the GAIA data. To avoid this potential data skewing, we filter out the stars that only appear in GAIA.

Other than the discrepancy with GAIA, the rest of the surveys match well with the trend of PS1, including the other surveys that make up the catalog that do not contain any data from PS1. For this reason we say that we trust the rest of our surveys.

## 4. DISTANCES AND HUBBLE DIAGRAM RESIDUALS

We fit SN Ia parameters  $x_1$  (stretch), color, and  $\mu$  (distance modulus) in SALT3. All share the same coefficients in  $\gamma$ ,  $\alpha$ , and  $\beta$ . Fig. 9 shows a comparison between TITAN and three other low-z surveys in stretch, color and, distance. We spatially match our SNe Ia against those of other surveys to get relative distance trends. We specifically compare against ZTF, DEBASS, and YSE. Notably, Foundation is absent from this comparison, this is because we did not have enough spatial matches of SNe Ia to say anything significant.

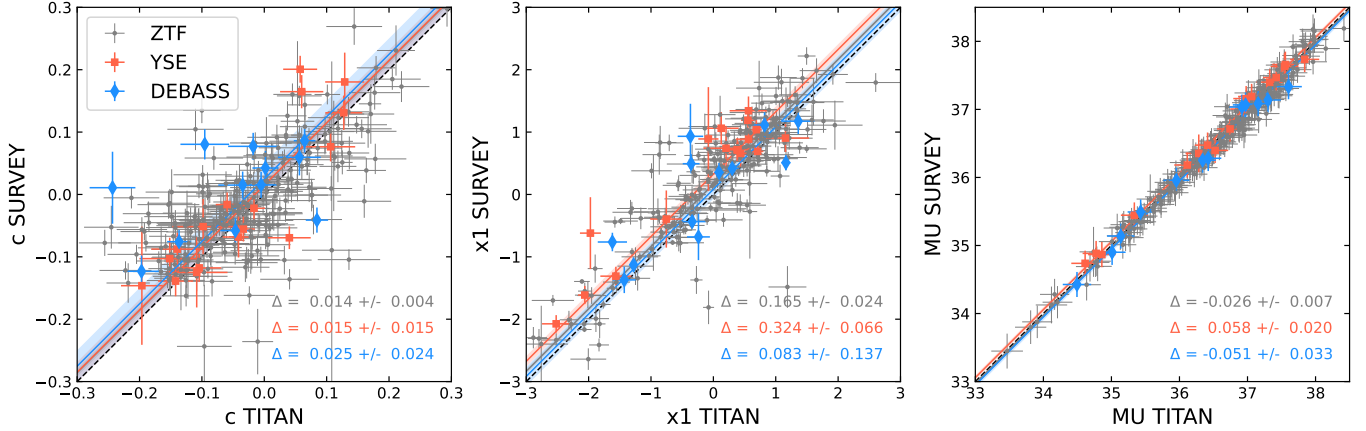


**Figure 9.** Comparison of TITAN SNe Ia with other modern low- $z$  surveys. TITAN light curves are presented in the companion paper Murakami et al. (2025). Compared against, ZTF DR2, DEBASS 0.5, YSE DR1. Plotted is Color, stretch ( $x_1$ ), and distance modulus (MU). We use a conservative color error cut of  $c_{\text{Err}} < 0.1$ , because there only being two bands in ATLAS means we can easily have a SNe Ia light curve without sufficient data in both bands. Due to the sizes of the datasets we are comparing against our matching with ZTF has over one thousand matches, while DEBASS and YSE have tens and hundreds of matches respectively. This is likely a major contributor to the significant errors on those comparisons in MU.

**Table 2.** Orange and cyan band zeropoint offset corrections and wavelength shifts for TITAN calibration. zeropoint offset corrections are in units of magnitude while wavelength shift is in units of Å.

Chip	$\Delta m_{\text{cyan}}$	$\Delta \lambda_{\text{cyan}}$	$\Delta m_{\text{orange}}$	$\Delta \lambda_{\text{orange}}$
	(mag)	(Å)	(mag)	(Å)
0	-	-	+0.176	+22
1	+0.017	+56	+0.013	+5
2	-	-	+0.019	+25
3	+0.028	+57	+0.017	+27
4	+0.014	+67	+0.002	-6
5	+0.011	+78	-0.003	-6
6	+0.011	+87	-0.003	+10
7	-0.010	+28	-0.004	-15
8	-0.017	+28	-0.031	-21

We demonstrate that our distance indicators (a significant benchmark) from our TITAN SNe Ia, after calibration are in line with other state of the art low- $z$  supernova experiments. This is one form of validation of our calibration and SN Ia dataset.

#### 4.1. ZTF

ZTF (Zwicky Transient Facility) SN Ia data release contains 2667 spectroscopically confirmed Type Ia SN with matching redshifts in the low- $z$  region ( $z < 0.3$ ) that pass initial cosmology cuts Rigault et al. (2025). This is one of the largest spectroscopically confirmed

low- $z$  supernova datasets to date. Note that ZTF has not completed their cosmology grade calibration, and acknowledge an offset in their dataset. We compare to ZTF as the only other low- $z$  sample with SNe on the same order of magnitude as TITAN.

#### 4.2. DEBASS

DEBASS (Dark Energy Bedrock All Sky Supernova program) has delivered the largest uniformly calibrated low- $z$  dataset of the southern sky to date (Sherman et al. 2025). They have already released 77 spectroscopically confirmed SNe Ia that pass cosmology cuts in DR 0.5 (Acevedo et al. 2025). DEBASS operates in the southern sky with a similar redshift range as TITAN ( $0.01 < z < 0.08$ ). Given that DEBASS operates off of DECam, which ATLAS is now calibrated to, this should enable excellent cross matching of SNe Ia once DEBASS DR1 is released and we can find hundreds of matches.

#### 4.3. YSE

YSE (Young Supernova Experiment) is comprised of data from ZTF and PS1, and contains 451 spectroscopically confirmed and cosmology grade SN Ia light curves. Their redshift range reaches a bit higher than TITAN ( $z < 0.5$ ), yet this is still a strong comparison for our low- $z$  dataset with dozens of matches in SN Ia (Aleo et al. 2023).

#### 4.4. Comparison of SALT3 Parameters

Fig. 9 gives us a high degree of confidence in our calibration of SNe Ia, and ATLAS’s ability to produce reliable light curves. Note that there is a cut on color error at  $\sigma_c < 0.1$  (see discussion in Murakami et al. 2025).

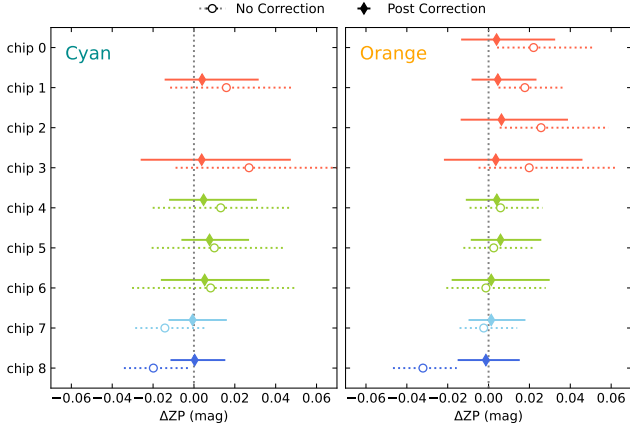


**Figure 10.**  $\Delta ZP$  offset in magnitude between real and synthetic ATLAS - DES transformed tertiary stars on x axis. The  $\Delta ZP$  value is the offset between chips and is corrected by the inter-chip correction. The error on the values is the result of a projection of the residuals from Fig. 5 into the  $\Delta ZP$  offset space, representing the scatter in residual. This error is dominated by the chromatic slope displayed in Fig. 6. Note, the data used for these calculations is completely independent from the stars used in calibration ('non-Refcat2' data), and are not in Refcat2. Can see that in both Orange and Cyan the  $\Delta ZP$  offset improves significantly after inter-chip correction. The error also improves in both cases, although substantially more in cyan as the slope gets significant corrections compared to orange. This plot shows a validation of inter-chip and chromatic slope calibration. Note, intra-chip correction is already applied to both pre and post correction data.

The left most plot in Fig. 9 shows the validity of our light curves through the small scatter of TITAN SNe Ia relative to other surveys. There is not a consistent positive or negative offset between TITAN and the other surveys indicating a lack of systematic difference.

There is an average offset of  $\sim 0.17$ ,  $0.32$ ,  $0.08$  for ZTF, YSE and DEBASS respectively, in the stretch parameter  $x_1$ . Though both ZTF and YSE offsets are significant, the offsets values significantly differ from each other, and the exact degree of systematic discrepancies is difficult to measure from this dataset alone. We will discuss this effect in Murakami et al. (2025). Color, on the other hand, is relatively consistent with some notable outliers. We believe the fact that there are only two filters in ATLAS produces these outliers, occasionally one of the filters will have too few measurements close to SNe Ia peak.

## 5. DISCUSSION

### 5.1. Validation with Independent Tertiary Catalog

One way we validate our calibration is using tertiary stars that are not contained in the Refcat2 catalog and

not used in our calibration calculations. These stars are in the DES catalog and we run ATLAS forced photometry on them (this is what is referred to as the 'non-refcat2' stars in Sec. 2). This provides a completely independent dataset for our validation. This means that from the perspective of ATLAS, these stars behave functionally the same as SNe Ia, a stellar object which the calibration has no prior knowledge of. Fig. 10 displays the effect our calibration has on these validation stars. Additionally, the error bars on these points represent the percentile range (16th percentile to 84th percentile) of the median value offset of a chip (essentially intrinsic scatter).

If our calibration were to be successful, we would expect to have a larger intrinsic scatter before corrections are applied, due to the slope of the residuals when projected in the offset space. This should be especially true in cyan band (see Fig. 6). Additionally, we would expect to see our zeropoint magnitudes close in on zero after calibration, due to the inter-chip correction.

Fig. 10 shows both of these to be true. Scatter, especially in cyan band (error bars), is reduced, and all of our offsets are closer to zero. Note chips 4c, 5c, 6c, all of whose scatter is reduced substantially with correction, these chips had some of the greatest initial chromatic slopes. Also note chip 8o, for example, whose delta zero point offset shifts substantially with the inter-chip correction. We find an initial offset of:  $0.017$  in orange, and  $0.016$  in cyan which get corrected to  $0.002$  and  $0.003$  respectively. Yielding an  $86\%$  reduction in orange band, and  $83\%$  reduction in cyan band offsets. We also find that the scatter is reduced by  $1\%$  in orange and  $28\%$  in cyan. This follows from our expected results, orange has minimal chromatic shift, while cyan's is large. This improvement demonstrates that we are able to correct for the discrepancy in residual slope with our filter wavelength shifts.

### 5.2. Validation with CALSPEC & DAWD Reference Stars

Another validation method we employ is using primary, and secondary stars to reproduce Fig. 10. We use a combined dataset of spectroscopic standards, CALSPEC (Bohlin et al. 2014) and DA-type faint White Dwarfs (hereafter DAWD; Boyd et al. 2025), to further validate our results and quantify systematic uncertainties. These spectroscopic standards, observed by *HST/STIS* with an absolute calibration to the physical units, provide a direct comparison of synthetic and observed spectra without the need of deriving the synthetic color-color transformation (Eq. A1). This independency, along with the broadly accepted use of the CALSPEC stars for photometric calibration, makes them an excel-

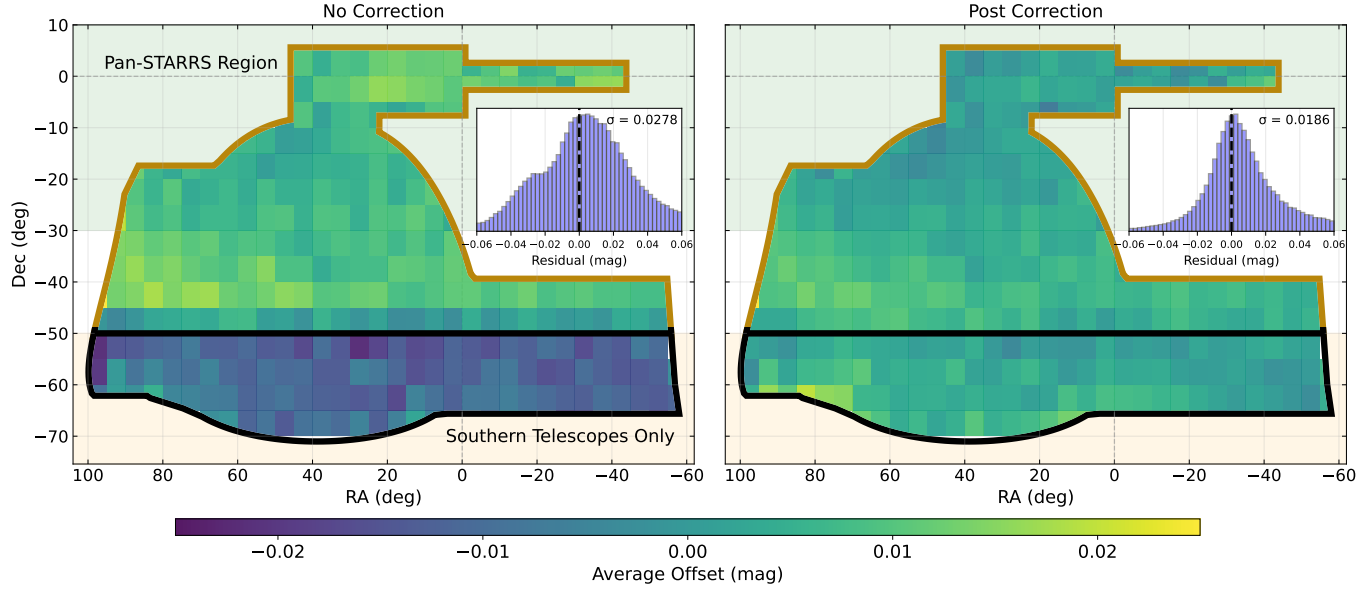


**Figure 11.** Heatmap of median offset as a function of spatial position. Correction applied here is inter-chip and chromatic shift. Clearly see that we improve the spatial dependence, and that the standard deviation improves. This is most noticeable around  $-50^{\circ}$  declination where the northern telescopes cut off. Can see that the histogram becomes substantially more gaussian after correction.

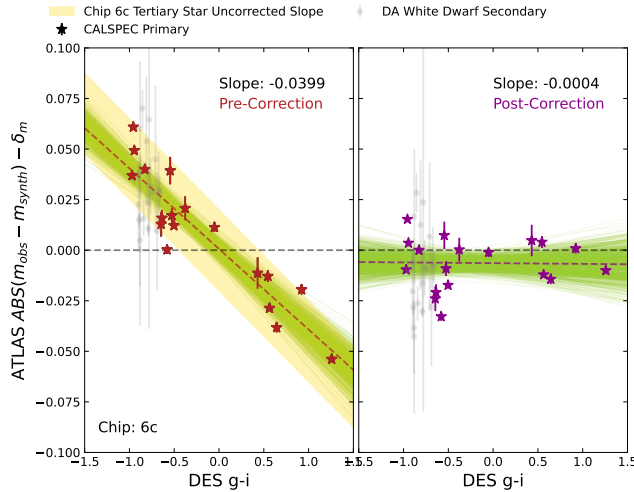


**Figure 12.** Absolute value of synthetic minus observed residuals of several CALSPEC stars, including C26202, and DAWD, on the y-axis in ATLAS cyan band. Here  $\delta_m$  is subtracted out. X axis is DES color in  $g - i$ . The many green lines represent random slope draws to account for covariance, shows a range of possible fitted slopes. The dotted lines are the median slope and the value displayed in Fig. 13. Post correction includes wave-shift and inter-chip offsets. The tertiary calibrator slope from Fig. 6 in chip 6c is overplotted pre-correction in gold. A small offset  $\delta_m$  is subtracted to account for the small numerical differences and make the shown values compatible with the absolute calibration of DES.

lent probe to test the possible systematics in the post-correction photometry in the TITAN dataset.

In addition to enabling an independent check of our tertiary star-based methods, the use of CALSPEC stars is relevant to the original calibrations of DES and ATLAS. DES uses a single primary calibrating star's spectra for its calibration to the absolute AB magnitude system, *HST CALSPEC C26202*. DES claims that, including systematic errors, the absolute flux is known at approximately the 1% level. DES generates these synthetic magnitude by integrating the official DES passband throughputs with one of standard spectra for C26202 from the HST CalSpec database (Bohlin et al. 2014). PS1, on the other hand, does not use a single CALSPEC star for its absolute calibration: instead, they rely on Ubercal from Schlafly et al. (2012) for the initial zeropoint calibration, which is then tied to the physical units using multiple CALSPEC standards (Magnier et al. 2020).

In Fig. 12, we present the measured offset between synthetic and ATLAS-observed photometry of chip c6 using CALSPEC and DAWD stars. An additional mmag-level offset  $\delta_m = m_{C26202}^{DES} - m_{C26202}^{synth}$  is subtracted to account for the difference between DES photometry of their absolute-scale calibrator, C26202, and our synthetic photometry. This is possibly due to the small, numerical effect from the difference in sub-sampling along the wavelength axis. We optimize a slope and offset  $\Delta ZP_i = \mathcal{A} \cdot (g - i)_i + \mathcal{B}$  (the purple line in Fig. 12) in our post-correction residual. We use the values of the slope ( $\mathcal{A}$ ) and the intercept ( $\mathcal{B}$ ) to quantify systematic uncertainties.

We see in Fig. 12 that, our corrections improves the chromatic effect. Our slope is reduced from -0.0399 to -0.0004. This is a validation of the methodology of our tertiary star calibration, showing we see nearly the exact same effective slope in primary and tertiary calibrators and are able to correct it. We do not present any orange band data for primary calibrators in this plot, orange band data already has minimal slope and our correction is extremely small. We show chip 6c an an excellent example validation of our filter-shift correction. We will discuss the resulting reduction of systematic uncertainty in Sec. 5.5.

### 5.3. Chromatic Effects

Our calibration corrects the chromatic effect, which we observe as a 0.005 – 0.045 mag-level difference (chip dependent) in zeropoint across the  $g - i$  color range corresponding to the TITAN SNe Ia color range. This effect is most notably seen in cyan band on the sitecam 02a telescope, as shown in Fig. 6.

Note that the slope is much larger (and not centered at zero) in cyan band, this suggests there is a filter problem, not CCD. Also note that chips 4c, 5c, and 6c, which are all on the same telescope, have the largest slopes, and get progressively larger with time. Chips 7c, 8c, are the newest telescopes and have the smallest cyan slope.

These patterns suggest to us several possible physical causes of this chromatic slope. First, quantum efficiency (QE) measurements between the telescope could be off in a systematic way. Second, the definition of the filter function in cyan could be different slightly than the physical filter. The trend in chips 4c, 5c, 6c suggests the possibility that something is repeatedly adjusted in the telescope that shifts the filter in some way. Resolving the physical cause of this chromatic effect will require further experimentation. The main point presented here, is that we are able to successfully correct this chromatic effect for cosmology by shifting the filter in wavelength.

### 5.4. Coordinate Dependence

When calibrating four independent telescopes it is important to verify there is no coordinate dependence (position dependence due to the different locations of the telescopes). There are two main spots we might expect coordinate dependence: at  $-50^\circ$  declination where the northern telescopes cut off, and  $-30^\circ$  declination where PS1 (the primary calibrating instrument of ATLAS) cuts off.

In Fig. 11 we can see, before calibration, there is a coordinate dependent offset at the northern telescope cutoff (the bluer region below  $-50^\circ$  dec). We are able to remove this offset with our inter-chip corrections as

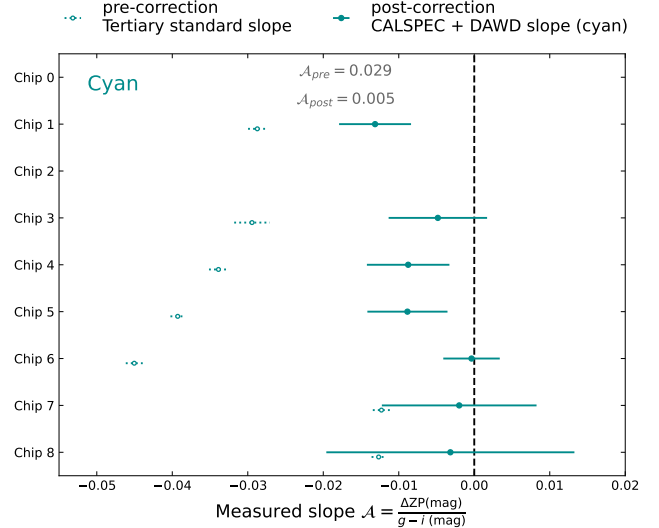


**Figure 13.** Systematic uncertainty in the cyan band due to the chromatic effect. X axis is the right side of Fig. 12, averaged across all of the random draw slope values. The pre-correction slopes come from the tertiary star slope found in Fig. 6. We find particularly large uncertainties for chips 7, 8 ( $\sim 0.010$  and  $\sim 0.016$  respectively). Our systematic uncertainty is calculated as the median of the slopes, across all chips pre, and post correction.

seen in the right side of the plot. In the histograms in Fig. 11, we find the scatter reduces substantially after our correction, and the histogram becomes more gaussian, not being biased as much to the positive residual. This is a numerical validation that the effect we see from the inter-chip correction is real.

Beyond this we notice no patch of the sky that is unique, there is a general uniformity above and below  $-50^\circ$  dec. Additionally, we do not see any effects above and below the PS1 region as we theorized may exist. This validates the initial Refcat2 zeropoint calibration per image.

### 5.5. Systematic Uncertainty

In this paper we present some initial systematic uncertainties due to calibration for cosmology. The first is the systematic uncertainty on the intra-chip correction. This is calculated as:  $\epsilon_{intra} = \sigma(\mathcal{O} - \mathcal{M})$ , where  $\mathcal{O}$  is the offset across all pixels in the chip and  $\mathcal{M}$  is the median of the chip (Sec. 3.1). To determine this systematic post calibration we subtract out our correction map from the real data observed ( $= \mathcal{O}$ –correction-map) in Fig. 3 and recalculate the standard deviation of the offset per pixel. In Tab. 3, we see a  $\sim 3$  mmag improvement across both bands, which is substantial given that the initial effect is only  $\sim 7$  mmag.

**Table 3.** Average systematic uncertainty values per filter before and after calibration. Values are in magnitude.

Systematic	orange		cyan		Description <sup>a</sup>
	Before	After	Before	After	
Intra-chip (pixel-to-pixel) variation	0.007	0.003	0.008	0.005	$\sigma(\Delta ZP_{\text{pixel}})$ in Fig. 3
Inter-chip (chip-to-chip) variation	0.017	0.002	0.016	0.003	$\sigma(\langle \Delta ZP \rangle_{\text{chip}})$ in Fig. 10
Chromatic Effect	0.004	0.003	0.029	0.005	Median slope ( $\mathcal{A}$ ) $\times$ SNe Ia color range (Sec. 5.5, Fig. 13)
Absolute Calibration	0.012	0.003	0.007	0.006	Median size of CALSPEC offsets, think Fig. 10 from Fig. 12
<b>Total</b>	<b>0.022</b>	<b>0.005</b>	<b>0.035</b>	<b>0.010</b>	

<sup>a</sup>Figures are cited here for reference purpose only, as they may only show measurements made before or after correction. We measure the same quantity before and after applying our correction models to quantify the reported values in this table.

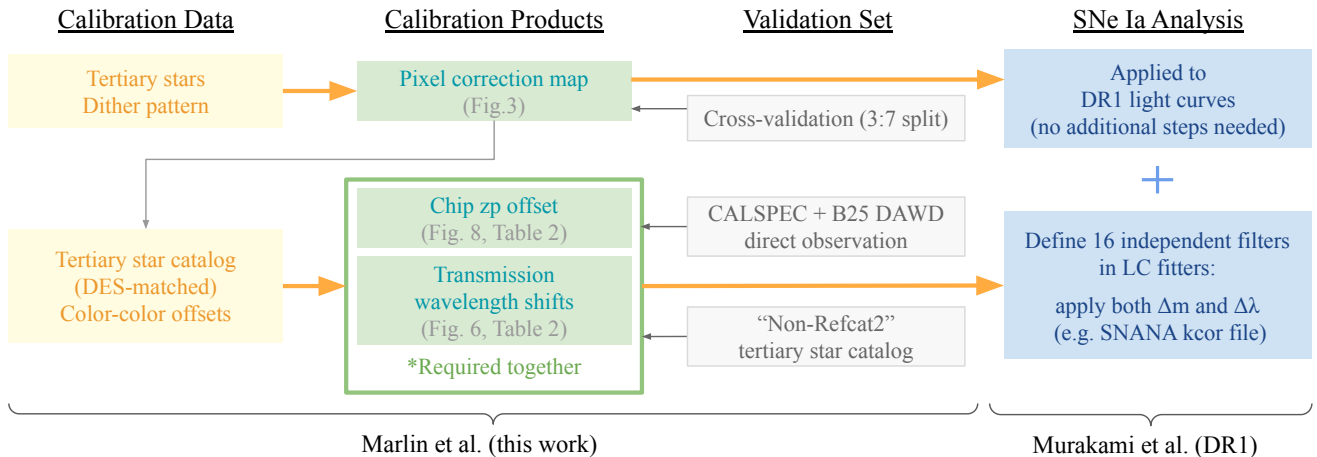


**Figure 14.** A summary of this work, products, and usage in future analysis. From left to right: dataset used in our analysis, calibration products (optimal calibration), dataset used to validate our calibration, and the methods to apply our calibration to SNe Ia light curve analysis (e.g., SALT3 fitting).

Second, the magnitude error floor, is the systematics on our inter-chip correction (Sec. 3.2). We find this by taking the standard deviation of the values presented in Fig. 10 for each filter. We repeat this on data before and after the inter-chip correction to verify that our calibration improves the magnitude error floor. Tab. 3 shows that our systematic uncertainty in error floor improves in both orange and cyan (by 15 and 13 mmag respectively).

Next, we quantify the systematic uncertainty related to the chromatic effect and our correction (wave shift) validated by our CALSPEC validation set (Sec. 3.2, 5.3). We define this systematic uncertainty as:  $\epsilon_{\text{chromatic}} = \mathcal{A} * \mathcal{SN}$ , where  $\mathcal{A}$  is the median slope across all chips, and  $\mathcal{SN}$  is the observed SNe Ia color range. This is practically propagated from the observed slope in the CALSPEC residuals using the SNe Ia color distribution ( $-0.97 \leq g - i \leq -0.11$  mag at  $2\sigma$  tails, covering 95% of the dataset) measured in Murakami et al. (2025).

Finally, we quantify our confidence in the absolute calibration of ATLAS using HST CALSPEC stars. We take the fitted offset (intercept of the slope at  $g - i$  color = 0) after the wave shift has been calculated ( $\mathcal{B}$ ). The systematic before calibration then:  $= \text{Median}(|\mathcal{B}|) - \delta_m$ . After calibration:  $= \text{Median}(|\mathcal{B}|) - (\text{interchip}) - \delta_m$ . This is essentially, an independent validation of only our inter-chip correction using primary calibrators. We specifically use data post-wave-shift correction for both the pre, and post absolute calibration systematic, as the wave-shift systematic is already contained within row 3 of Tab. 3 (Sec. 5.5, Fig. 13). We find a 9 mmag, and 1 mmag improvement for orange and cyan bands respectively.

Before our correction, the median slopes for each filter is  $\frac{\text{Residual}}{g-i} \sim 0.029, 0.004$  for cyan<sup>10</sup> and orange band,

<sup>10</sup>The slope for cyan band varies by a factor of a few between detectors. We use the median values for each filter as a repre-

respectively (see Fig. 6). This corresponds to  $\sim 0.026$  and  $\sim 0.003$  mag-level changes in the zeropoint across the color range of SNe Ia. The slope is consistent across our tertiary catalog and the primary, CALSPEC validation set. After applying our corrections derived from the tertiary star catalog, the remaining slope in the CALSPEC stars become considerably small (0.005), making the systematic uncertainty consistent across filters  $0.005 \frac{\text{mag}}{g-i \text{ mag}} \times (-0.11 - (-0.97)) \text{ mag} \approx 0.0043 \text{ mag}$ .

Tab. 3 demonstrates that before our correction, we have a total systematic of 22mmag, 35mmag in orange and cyan bands respectively. After calibration we are able to reduce these numbers to 5mmag, 10mmag respectively, presenting a 77% and 71% reduction in systematics respectively. This is the lowest relevant sensitivity for TITAN cosmology. For reasons discussed in Murakami et al. (2025), we find that in *SNANA* we must add a 10 mmag error floor to our TITAN SNe Ia already. This implies that our additional systematics from calibration are on a scale to not significantly impact our SN Ia dataset.

### 5.6. Usage and Data Tools

The substantial work presented here can be reduced down to a simple calibration pipeline shown in Fig. 14. This flow chart shows our three calibration outputs, the pixel correction map (intra-chip), chip ZP offset (inter-chip) and transmission wavelength shifts. For the chip zp offsets and the transmission wavelength shifts these values can be lifted directly from Tab. 2 and applied to any ATLAS photometry files using the tools presented in the *ATLAST* package of the data release. The pixel correction map produced here will also be available for download with DR1, and can be applied with a single line of python code from *ATLAST*.

Fig. 14 also shows the validation sets used. The chip zp offset and transmission wavelength shift validations are discussed further in Sec. 5.2 and Sec. 5.1, while the pixel correction map validation map is presented in App. C. For direct application to SN Ia light curves please see Murakami et al. (2025). All tools and calibration data can be downloaded from: <https://titan-snia.github.io>.

## 6. CONCLUSION

SNe Ia are a well proven tool for measuring relative distances for use in cosmology. Until now, most major SN Ia cosmology surveys have relied on the same 200 low-z SNe Ia. TITAN will fix this, providing the

sensative value solely for the comparison with the post-correction size.

largest, independent, spectroscopically confirmed low-z SNe Ia dataset to date. TITAN, which uses the ATLAS all sky survey, must be internally calibrated across the entire network using literature proven standards before it can be used in cosmology. That calibration has been presented in this paper.

We conduct a relative calibration between ATLAS and DES, a well measured survey that contains data inside and outside of PS1 (the primary calibrating instrument of ATLAS). In order to do this calibration we produced three distinct tertiary calibration star catalogs (Sec. 2.1). The first ('color-blind'), containing a color uniform random sample from across the DES footprint, was produced matching Refcat2 stars with DES and then running forced photometry on ATLAS. The second ('blue'), containing a color sample that is biased substantially blue to match the color range of low-z SNe Ia and account for the redder nature of Milky Way stars, is produced in the same method as the first. We re-sample these first two catalogs to produce a new dataset, uniform in color, to account for the bluer nature of the SNe Ia and the naturally redder nature of Milky Way stars. The final catalog ('non-Refcat2'), is a subset of stars that do not exist within Refcat2 (reverse matched), but are matched with DES before requesting forced photometry from ATLAS. This catalog provides a completely independent dataset that mimics the behavior of SNe Ia in ATLAS. We also generate synthetic data using CALSPEC and NGSL standard stars, produced via a modification of Dovekie.

We examine pixel to pixel variations in each CCD and filter (intra-chip). We find most are consistent well below the 0.01 level, with the exception of chip 8o, where we notice a significant vignetting pattern (Fig. 3). To account for the variations in pixel we build a correction map. This is produced by binning the data, smoothing at an optimally calculated pixel radius (see App. C), then remapping to the 10,000 x 10,000 pixel CCD. We separately produce a map for each chip filter combination.

On a larger scale we create a correction between each CCD and filter (inter-chip). To do this we calculate the vertical shift in DES - ATLAS transformation and stellar color between the observed data and our synthetically produced data (Fig. 5). The offset produced here constitutes our inter-chip correction. Notably, the synthetic - real residual is not flat at a constant value above or below 0, there is a slope (Fig. 6). This means that there is a color dependence on our transformation, especially in the cyan band. We find that we can correct for this by applying a shift in the wavelengths of the filters, as has been done previously in the literature (Fig. 7).

This shift corrects for the slope and reduces the need to inflate the systematic uncertainty to account for it. Fig. 11 shows a validation of our inter-chip correction.

We validate our corrections in three ways. 1). An independent tertiary star catalog (Fig. 10), 2). independent primary and secondary absolute calibrators HST CALSPEC, and DAWD stars (Fig. 12), 3). distance moduli of cross-matched SNe Ia (Fig. 9). All validation efforts point to improved consistency overall and reduced systematics (Tab. 3).

The calibration presented here serves as a baseline internal validation for the upcoming cosmological analysis, that will result from what we are releasing as TITAN DR1. The data release and all associated tools will be presented on the TITAN website at: <https://titan-snia.github.io>. The light curves and simulations will be presented in Murakami et al. (2025) and Tweddle et al. (2025) respectively.

## ACKNOWLEDGEMENTS

We would like to thank the ATLAS team for assistance in gathering massive amounts of forced photometry and for their conversations about the difference imaging pipeline and nuances of the telescopes.

We thank the Hariri Institute at Boston University, for their generous funding contributions to this project.

D.O.J. acknowledges support from NSF grants AST-2407632, AST-2429450, and AST-2510993, NASA grant 80NSSC24M0023, and HST/JWST grants HST-GO-17128.028 and JWST-GO-05324.031, awarded by the Space Telescope Science Institute (STScI), which is operated by the Association of Universities for Research in Astronomy, Inc., for NASA, under contract NAS5-26555.

## APPENDIX

### A. MULTI-COLOR JOINT LIKELIHOOD ANALYSIS

In Sec. 3.2, we fit a single offset value to an ATLAS filter so that the empirical ATLAS-DES filter transformation matches synthetic prediction. This transformation is color-dependent, and there are multiple possible combinations of DES filters (e.g., ATLAS-o $\rightarrow$ DES-g as a function of color DES-g-DES-i). Each of the combination can be simultaneously evaluated to form a joint likelihood, and we describe the formalism of our likelihood function and the process to prepare necessary quantities below.

First, assuming that the DES filters and their star catalog values are well-calibrated, we obtain an ATLAS offset for each (i-th) star as the following:

$$\Delta_{i, x1, x2, y1, y2} = m_{i,y1}^{\text{ATLAS}} - m_{i,y2}^{\text{DES}} - f_{y1 \rightarrow y2}^{\text{synth}}(m_{i,x1}^{\text{DES}} - m_{i,x2}^{\text{DES}}) , \quad (\text{A1})$$

where  $m$  represent observed magnitudes of stars, with subscripts  $y1$  for the ATLAS band of interest and  $x1, x2, y2$  for DES bands we use as a reference. Considering the overlaps of the sensitivity functions, we use the combinations of filters shown in Table 4. We note that there are two exceptions in the listed combinations: the dataset obtained with  $(y1, y2, x1, x2) = (c,g,g,r)$  is linearly identical to  $(c,r,g,r)$ , and it causes the covariance matrix we describe later to be nearly singular. To avoid this issue and considering that it adds nearly no information, we exclude such combination. Similarly, another combination for the orange filter  $(o,i,r,i)$  is excluded. The synthetic transformation function between ATLAS filter  $y1$  and DES filter  $y2$   $f_{y1 \rightarrow y2}^{\text{synth}}$  is obtained by fitting a third-order polynomial to a fully synthetic data  $m'$ ,

$$y^{\text{fit}} = f_{\text{synth}} = \text{Poly}_3(x), \quad x = m'_{x1} - m'_{x2}, \quad y = m'_{y1} - m'_{y2} . \quad (\text{A2})$$

After evaluating  $\Delta_i$  for each of the combination, we obtain a vector of offsets  $\mathbf{r}_i = (\Delta_{i1}, \Delta_{i2}, \dots, \Delta_{i5})^\top$ . Due to repeated uses of data, these measurements are not independent from each other, and we quantify that effect by constructing a filter-to-filter covariance matrix for each star. Propagating uncertainties from each observed quantity

**Table 4.** Combinations of filters used for the offset analysis.

#	ATLAS- <i>c</i>				ATLAS- <i>o</i>			
	<i>y</i> 1	<i>y</i> 2	<i>x</i> 1	<i>x</i> 2	<i>y</i> 1	<i>y</i> 2	<i>x</i> 1	<i>x</i> 2
1	ATLAS- <i>c</i>	DES- <i>g</i>	DES- <i>g</i>	DES- <i>r</i>	ATLAS- <i>o</i>	DES- <i>r</i>	DES- <i>g</i>	DES- <i>r</i>
2	ATLAS- <i>c</i>	DES- <i>g</i>	DES- <i>r</i>	DES- <i>i</i>	ATLAS- <i>o</i>	DES- <i>r</i>	DES- <i>r</i>	DES- <i>i</i>
3	ATLAS- <i>c</i>	DES- <i>g</i>	DES- <i>g</i>	DES- <i>i</i>	ATLAS- <i>o</i>	DES- <i>r</i>	DES- <i>g</i>	DES- <i>i</i>
4	ATLAS- <i>c</i>	DES- <i>r</i>	DES- <i>r</i>	DES- <i>i</i>	ATLAS- <i>o</i>	DES- <i>i</i>	DES- <i>g</i>	DES- <i>r</i>
5	ATLAS- <i>c</i>	DES- <i>r</i>	DES- <i>g</i>	DES- <i>i</i>	ATLAS- <i>o</i>	DES- <i>i</i>	DES- <i>g</i>	DES- <i>i</i>

in Eq. A1, we obtain a  $5 \times 5$ -matrix:

$$[\Sigma_i]_{jk} = \underbrace{\sigma_{y_{1j}}^2 + \sigma_{y_{2j}}^2 \delta(y_{2j}, y_{2k})}_{\text{ATLAS } y_1 - \text{DES } y_2 \text{ error}} + \underbrace{f'_k \sigma_{y_{2j}}^2 [\delta(y_{2j}, x_{1k}) - \delta(y_{2j}, x_{2k})] + f'_j \sigma_{y_{2k}}^2 [\delta(y_{2k}, x_{1j}) - \delta(y_{2k}, x_{2j})]}_{y_2 - \text{color}} + \underbrace{f'_j f'_k \sigma_{x_{1j}}^2 [\delta(x_{1j}, x_{1k}) - \delta(x_{1j}, x_{2k})] - f'_j f'_k \sigma_{x_{2j}}^2 [\delta(x_{2j}, x_{1k}) - \delta(x_{2j}, x_{2k})]}_{\text{color} - \text{color}}. \quad (\text{A3})$$

Using this covariance matrix, we obtain an appropriate weights between each measurement within  $\mathbf{r}_i$  and collapse it into a single, representative offset value per star (generalized least-square estimation; GLS):

$$\bar{r}_i = \frac{\mathbf{1}^\top \Sigma_i^{-1} \mathbf{r}_i}{\mathbf{1}^\top \Sigma_i^{-1} \mathbf{1}}, \quad \sigma_{\bar{r},i}^2 = \frac{1}{\mathbf{1}^\top \Sigma_i^{-1} \mathbf{1}} \quad (\text{A4})$$

where  $\sigma_{\bar{r},i}^2$  is the variance for  $\bar{r}_i$ , and  $\mathbf{1} = (1, 1, \dots, 1)^\top$  is an all-one vector.

The obtained per-star offset value  $\bar{r}_i$  and its variance  $\sigma_{\bar{r},i}^2$  is then used to evaluate our likelihood, which accounts for possible combinations of filters, their uncertainties, covariances, and overlapping use of data across such combinations:

$$\ln \mathcal{L}(\Delta_f, \sigma_{\text{int},f}) = \sum_i^{N_{\text{star}}} -\frac{1}{2} \left[ \frac{(\bar{r}_i - \Delta_f)^2}{\sigma_{\bar{r},i}^2 + \sigma_{\text{int}}^2} + \ln(2\pi\sigma_{\bar{r},i}^2 + 2\pi\sigma_{\text{int}}^2) \right]. \quad (\text{A5})$$

This formula evaluates the likelihood of proposed offset for the ATLAS filter  $\Delta_f$  (mag) against the par-star residual  $\bar{r}_i$  (mag) for each  $i$ -th star, which is derived from multiple combinations of filters between ATLAS and DES. We simultaneously measure the star-to-star intrinsic scatter  $\sigma_{\text{int}}$ .

## B. PROFILE LIKELIHOOD FOR WAVELENGTH OFFSET

### C. OPTIMAL SMOOTHING RADIUS DETERMINATION:

To determine our optimal smoothing radius we trained a model on 70% of the data from our calibration stars and then validated it with the remaining 30%. This process is done on each chip/ filter combo and the split is regenerated randomly four times for each combo. This results in Fig. 15, which shows the reduced chi squared as a function of smoothing radius. You can see that most of the chips are in the 250 - 750 pixel smoothing radius range for optimal reduced chi squared.

Our model functions as follows: it bins the data into 50x50 pixel chunks. It then convolves the binned data with a gaussian kernel (it ignores edge effects as these have a higher likelihood of being inaccurate by definition). Our model then uses the large scale structure of the CCD to correct for systematic offsets in the photometric residuals across the chip.

We used Fig. 15 to determine a median minimum chi squared across all chips, for which smoothing radius we should use for our correction model. We then apply the smoothing to the dataset which provides a correction to the dataset

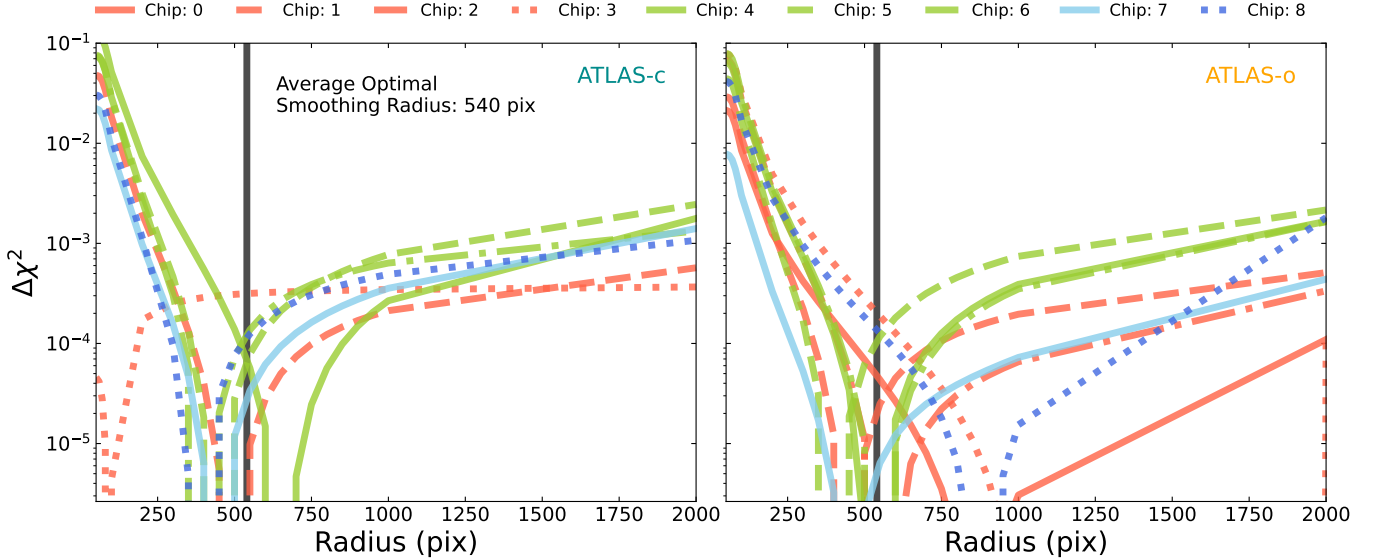


**Figure 15.** Cross validation plot of normalized chi squared vs smoothing radius in pixels. You can see the smoothing radius that minimizes the chi squared is focused around 540 pixels. We would rather slightly over bin (thus under correct) than under bin which would result in over correcting leading to potentially misleading and unrealistic trends. The y axis is reduced chi squared minus the minimum chi squared for each chip filter combo.

specifically correcting the chip 8 data without changing the rest of the chips data. This produces our intra-chip correction.

## REFERENCES

- Abbott, D. C. T. M. C., Acevedo, M., Aguena, M., et al., 2024a, *The Astrophysical Journal Letters*, 973, 1, L14  
 Abbott, D. C. T. M. C., Acevedo, M., Aguena, M., et al., 2024b, *The Astrophysical Journal Letters*, 973, 1, L14  
 Acevedo, M., Sherman, N. F., Brout, D., et al., 2025, *The Dark Energy Bedrock All-Sky Supernova Program: Cross Calibration, Simulations, and Cosmology Forecasts*, arXiv:2508.10877  
 Aleo, P. D., Malanchev, K., Sharief, S., et al., 2023, *ApJS*, 266, 1, 9, arXiv:2211.07128  
 Bechtol, K., et al., 2025, *Dark Energy Survey Year 6 Results: Photometric Data Set for Cosmology*, no journal information available  
 Bohlin, R. C., Gordon, K. D., Tremblay, P. E., 2014, *PASP*, 126, 942, 711, arXiv:1406.1707  
 Boruah, S. S., Hudson, M. J., Lavaux, G., 2020, *MNRAS*, 498, 2, 2703, arXiv:1912.09383  
 Boyd, B. M., Narayan, G., Mandel, K. S., et al., 2025, *MNRAS*, 540, 1, 385, arXiv:2412.08809  
 Brout, D., Scolnic, D., Popovic, B., et al., 2022, *ApJ*, 938, 2, 110, arXiv:2202.04077  
 Brout, D., Taylor, G., Scolnic, D., et al., 2022, *The Astrophysical Journal*, 938, 2, 111, ISSN 1538-4357  
 Brout, D., Taylor, G., Scolnic, D., et al., 2022, *ApJ*, 938, 2, 111, arXiv:2112.03864  
 Brown, B. A. A. H. S. K. P. P. T., Peter J., 2014, 354, 1, 89  
 Burke, D. L., Rykoff, E. S., Allam, S., et al., 2017, *The Astronomical Journal*, 155, 1, 41  
 Chen, P., Dong, S., Kochanek, C. S., et al., 2022, *ApJS*, 259, 2, 53, arXiv:2011.02461  
 DESI Collaboration, Abdul Karim, M., Aguilar, J., et al., 2025, *PhRvD*, 112, 8, 083515, arXiv:2503.14738  
 Filippenko, A. V., 2005, *Type Ia Supernovae and Cosmology*, 97–133, Springer Netherlands, Dordrecht  
 Foley, R. J., Koekemoer, A. M., Spergel, D. N., et al., 2018a, arXiv e-prints, arXiv:1812.00514, arXiv:1812.00514  
 Foley, R. J., Scolnic, D., Rest, A., et al., 2018b, *MNRAS*, 475, 1, 193, arXiv:1711.02474  
 Ganeshalingam, M., Li, W., Filippenko, A. V., et al., 2010, *The Astrophysical Journal Supplement Series*, 190, 2, 418  
 Hamuy, M., Phillips, M. M., Suntzeff, N. B., et al., 1996, *AJ*, 112, 2438, arXiv:astro-ph/9609063  
 Hicken, M., Challis, P., Jha, S., et al., 2009a, *ApJ*, 700, 1, 331, arXiv:0901.4787

- Hicken, M., Challis, P., Kirshner, R. P., et al., 2012, ApJS, 200, 2, 12, arXiv:1205.4493
- Hicken, M., Wood-Vasey, W. M., Blondin, S., et al., 2009b, ApJ, 700, 2, 1097, arXiv:0901.4804
- Jha, S., Kirshner, R. P., Challis, P., et al., 2006, AJ, 131, 1, 527, arXiv:astro-ph/0509234
- Koleva, M., Vazdekis, A., 2012, *Astronomy and Astrophysics*, 538, A143, ISSN 1432-0746
- Krisciunas, K., Contreras, C., Burns, C. R., et al., 2017, AJ, 154, 5, 211, arXiv:1709.05146
- Lyman, R., Cherubini, T., Businger, S., 2020, *Monthly Notices of the Royal Astronomical Society*, 496, 4, 4734, ISSN 0035-8711,  
<https://academic.oup.com/mnras/article-pdf/496/4/4734/33503937/staa1787.pdf>
- Magnier, E. A., Schlafly, E. F., Finkbeiner, D. P., et al., 2020, ApJS, 251, 1, 6, arXiv:1612.05242
- Murakami, Y., Tweddle, J., Marlin, E., et al., 2025, TITAN: Type Ia Supernova Trove from ATLAS in the Nearby Universe. Overview and the data release of 10,000 light curves, in preparation
- Phillips, M. M., 1993, ApJL, 413, L105
- Popovic, B., Kenworthy, W. D., Ginolini, M., et al., 2025, arXiv e-prints, arXiv:2506.05471, arXiv:2506.05471
- Riess, A. G., Kirshner, R. P., Schmidt, B. P., et al., 1999, AJ, 117, 2, 707, arXiv:astro-ph/9810291
- Riess, A. G., Yuan, W., Macri, L. M., et al., 2022, ApJL, 934, 1, L7, arXiv:2112.04510
- Rigault, M., Smith, M., Goobar, A., et al., 2025, A&A, 694, A1, arXiv:2409.04346
- Rubin, D., Aldering, G., Betoule, M., et al., 2025, ApJ, 986, 2, 231, arXiv:2311.12098
- Rykoff, E. S., Tucker, D. L., Burke, D. L., et al., 2023, Sanderson, R. E., Hickox, R., Hirata, C. M., Holman, M. J., Lu, J. R., Villar, A., 2024, arXiv e-prints, arXiv:2404.14342, arXiv:2404.14342
- Schlafly, E. F., Finkbeiner, D. P., Jurić, M., et al., 2012, *The Astrophysical Journal*, 756, 2, 158
- Scolnic, D., Brout, D., Carr, A., et al., 2022a, ApJ, 938, 2, 113, arXiv:2112.03863
- Scolnic, D., Brout, D., Carr, A., et al., 2022b, ApJ, 938, 2, 113, arXiv:2112.03863
- Scolnic, D., Casertano, S., Riess, A., et al., 2015, ApJ, 815, 2, 117, arXiv:1508.05361
- Sherman, N. F., Acevedo, M., Brout, D., et al., 2025, arXiv e-prints, arXiv:2508.10878, arXiv:2508.10878
- Stahl, B. E., Zheng, W., de Jaeger, T., et al., 2019, MNRAS, 490, 3, 3882, arXiv:1909.11140
- Tang, X. T., Brout, D., Karwal, T., Chang, C., Miranda, V., Vincenzi, M., 2025, Uniting the Observed Dynamical Dark Energy Preference with the Discrepancies in  $\Omega_m$  and  $H_0$  Across Cosmological Probes, arXiv:2412.04430
- Tonry, J. L., Denneau, L., Flewelling, H., et al., 2018, *The Astrophysical Journal*, 867, 2, 105
- Tonry, J. L., Denneau, L., Heinze, A. N., et al., 2018, PASP, 130, 988, 064505, arXiv:1802.00879
- Tripp, R., 1998, A&A, 331, 815
- Tweddle, J., Murakami, Y., Marlin, E., et al., 2025, TITAN: The Type Ia Supernova Trove from ATLAS in the Nearby Universe - Simulations and Bias Corrections, in preparation
- Vincenzi, M., Brout, D., Armstrong, P., et al., 2024, The Dark Energy Survey Supernova Program: Cosmological Analysis and Systematic Uncertainties, arXiv:2401.02945